Solid State Science and Technology, Vol. 32, No. 2 (2024) 163-184
https://doi.org/10.66514/ssst32-2-163-184

Simulation of Combined Metal-Hydrogenous-Composite Materials for Multilayer Shielding of High Energy Proton Radiation Using Monte Carlo Code PHITS

Fitrotun Aliyah[1,2], Azhar Abdul Rahman[1,], Yasmin Md Radzi[1], Yoon Tiem Leong[1] Imam Kambali[3]*

[1]School of Physics, Universiti Sains Malaysia, 11800, Minden, Penang, Malaysia

[2]Department of Nuclear Engineering and Engineering Physics, Universitas Gadjah Mada, 55281, Sleman, Yogyakarta, Indonesia

[3]Research Center for Accelerator Technology, National Research and Innovation Agency, 55281, Sleman, Yogyakarta, Indonesia

** Corresponding author; email: arazhar@usm.my*

Received: 22 August 2024 / Accepted: 15 November 2024

ABSTRACT

Multilayer shielding scenarios for proton radiation with secondary neutron and gamma radiation have been investigated using the Monte Carlo simulation method through Particle Heavy Ion Transport System (PHITS). This research aims to evaluate shielding effectiveness with variations of layer structure from a combination of metal, hydrogenous, and composite materials and determine the optimum shielding thickness that follows the radiation protection standard. The simulation uses a 230 MeV proton source, 1 nA beam current, and water target as the tissue equivalent. The shielding consists of three layers of beam dump from iron (Fe), Portland concrete, and Borated Polyethylene (BPE) materials. The parameters measured in this study are fluence distribution, ambient dose equivalent H*(10) rate, and induced radioactivity assessment. The simulation results show that the configuration with the iron material on the first layer can attenuate high proton and neutron radiation energy and reduce energy effectively. However, it produces a high dose build-up effect with higher gamma radiation from inelastic scattering reaction, which causes the consideration of additional radiation exposure to the gantry room. On the other hand, placing Fe in the second layer between BPE and concrete (BPE-Fe-concrete or Concrete-Fe-BPE) should be an excellent option with modest H*(10) and minimum gamma exposure in front of shielding. The estimation of induced radioactivity in the multilayer shielding was performed by predicting a neutron capture and neutron spallation reaction process. The optimum thickness of each layer for the scenario of 1 m distance from the target is BPE (30 cm), Fe (90 cm), and concrete (110 cm).

Keywords: multilayer shielding; proton; neutron; Monte Carlo; PHITS

INTRODUCTION

Shielding is a critical point in constructing nuclear and health facilities for diagnostics, radiotherapy, and nuclear medicine. The role of shielding is to protect workers and the public from radiation hazards to organs. The selection of shielding materials and structures is vital because it will affect radiation facilities' safety, economic, and land requirements. One of the radiotherapy modalities currently developing massively is proton therapy [1]. Proton therapy has become an established cancer treatment modality in radiation oncology and has many advantages over conventional radiotherapy using X-rays or photons [2]. Based on the Particle Therapy Co-Operative Group (PTCOG) data, proton therapy facilities that are in the operating, under construction, and planning phases have an energy range of 60 MeV – 330 MeV, with 43% of all facilities having 250 MeV and 39% of the total facilities has 230 MeV [3]. It is known that the interaction of high-energy protons with matter produces secondary radiation, neutrons, and gamma rays [4,5], which requires great care in developing radiation shielding for both types of radiation. The Monte Carlo method has been widely used to optimally design neutron and gamma-ray shielding. In 2017, Hu et al. developed a new shielding material for The Compact Accelerator-driven Neutron Source (CANS) with polyethylene and Pb using Monte Carlo and PHITS application [6], and Prusator et al. performed a shielding assessment on the Mevion S250 Proton therapy unit using the Monte Carlo model [1]. In 2020, Lai et al. calculated the shielding design for Boron Neutron Capture Therapy from 30 MeV proton using the Monte Carlo method [7]. Wang et al. designed shielding for compact proton synchrotron-based therapy using FLUKA [8]. The same year, Hu et al. simulated composite shielding for neutrons and gamma rays using MCNP and genetic algorithm (GA) [9,10]. Then in 2021, Augusto et al. conducted a shielding optimization study for the TRIUMF-AIREL proton accelerator facility using FLUKA [11], Gonzalo et al. conducted verification of shielding in the commissioning of the Compact Proton Therapy Centre [12], and Ma et al. used MCNP to optimize the shielding compact accelerator-driven neutron sources (CANS) design [13]. In previous research, proton therapy shielding was designed using one layer of concrete material and then developed using a combination of iron-concrete to reduce the shielding thickness. In comparison, composite materials with a high absorption cross-section for neutrons and gamma rays are indicated can increase the effectiveness of shielding performance. Therefore, the shielding thickness will decrease and meet radiation protection standards. This study will simulate using metal-hydrogenous -composites materials as a multilayer shielding material for high-energy protons that produce secondary radiation of fast neutrons and gamma rays.

MATERIALS AND METHODS

A physical basis for proton interaction mechanism and multilayer shielding method

The interaction of protons with matter will produce three collision schemes: coloumb interactions with atomic electrons, coloumb interactions with atomic nuclei, and nuclear interactions [4,5,14,15]. Coloumb proton interaction with atomic electrons will cause protons to lose energy through ionization also atomic excitation and eventually stop. Meanwhile, the coloumb interaction between protons when approaching the atomic nucleus will cause inelastic coloumb scattering, producing a proton beam penumbra. And the interaction of protons with the nucleus will cause a non-elastic collision, generating secondary radiation of neutrons and gamma rays. High-energy

protons interacting with targets will produce fast neutrons and high-intensity gamma rays. The interaction between the neutron and shielding material for fast neutron shielding consists of inelastic scattering, elastic scattering, absorption, and capture[10]. Inelastic scattering causes the neutron energy to decrease from fast neutrons (>1 MeV) to an intermediate level (10^{-5} MeV – 1 MeV). When the energy is below the intermediate threshold, elastic scattering will slow the neutron until it reaches a thermal level (0.025 MeV). Finally, the neutron is captured by the shielding material. In this context, absorption is the same as capture because fission is extremely unlikely in this scenario. As for gamma rays, the interactions that occur include Compton scattering, pair production, and photoelectric [10]. The whole interaction process is shown in Figure 1.

Shielding aims to protect workers and the public from radiation hazards by reducing energy and absorbing particles and their secondary radiation. Multilayer shielding uses a combination of structures and components of shielding material to withstand radiation to have a better effect than traditional shielding with one type of material so that the shielding thickness significantly reduces.

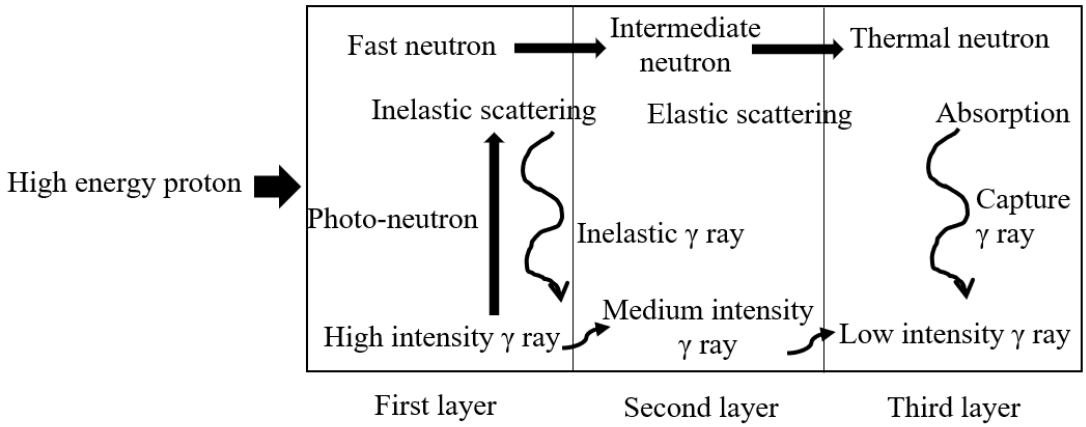

Figure 1. Interaction of radiation in multilayer shielding, adapted from [10]

Materials for multilayer shielding

The multilayer shielding material combines metal (Fe) with its various isotopes, hydrogenous materials from Portland concrete, and composite materials from Borated polyethylene (BPE). The material's density and atomic fraction composition are listed in Table 1. The multilayer structural design scenarios will be varied in 6 arrangements and one scenario using a single layer from concrete material as a comparison, as shown in Table 2. The total shielding thickness is 100 cm, with the thickness of each material being 40 cm for Fe, 40 cm for Portland concrete, and 20 cm for BPE. After getting the simulation results of the arrangement with the best shielding effectiveness, the study will continue to simulate the optimum thickness of each material by varying the percentage of Fe, concrete, and BPE thicknesses.

Table 1. Shielding materials properties

Material	Density (g/cm^3)	Composition (atomic fraction)
Iron, Fe	7.8	1.00
Concrete [12]	2.3	
^{1}H		0.023
^{12}C		0.019
^{16}O		0.530
^{27}Al		0.034
^{28}Si		0.337
^{40}Ca		0.044
^{56}Fe		0.014
Borated Polyethylene (BPE) [16]	0.97	
^{1}H		0.644
^{12}C		0.322
^{16}O		0.022
^{10}B		0.003
^{11}B		0.011

Table 2. Multilayer shielding structure

Scenario	Material	Dimension (cm)
1	Fe-Concrete-BPE	40-40-20
2	Fe-BPE-Concrete	40-20-40
3	Concrete-Fe-BPE	40-40-20
4	Concrete-BPE-Fe	40-20-40
5	BPE-Fe-Concrete	20-40-40
6	BPE-Concrete-Fe	20-40-40
7	Concrete	100

Geometry layout

The geometry arrangement between the source, target, and shielding is shown in Figure 2. The source is a 230 MeV monoenergetic proton with a beam current of 1 nA. The reason for choosing proton energy is that almost half of the compact proton therapies installed worldwide use an energy range of 230 MeV. The target is water (1 g/cm^3), a tissue-equivalent material with a thickness of 5 cm. The distances between the proton source and the target and the target with the shielding are 5 cm and 10 cm, respectively. While the detector is placed right behind the shielding.

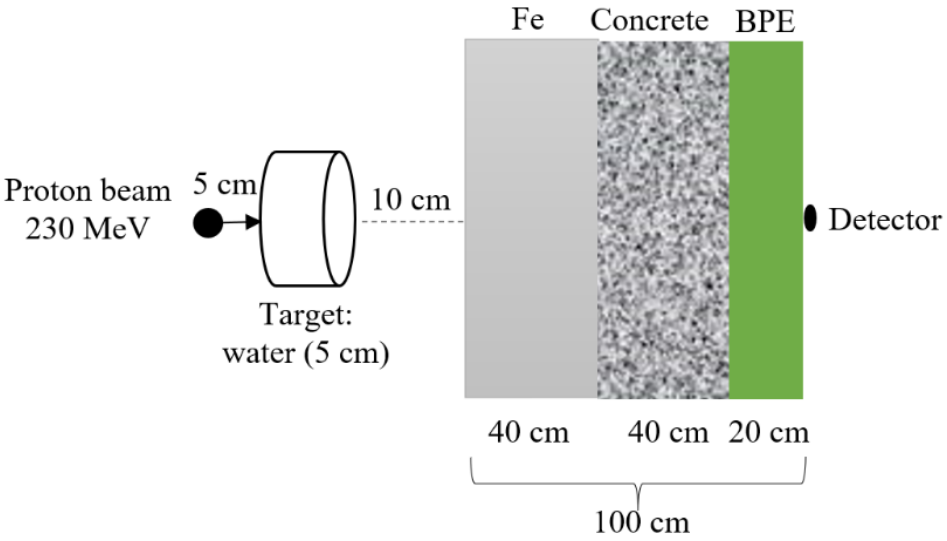

Figure 2. Geometry layout for source, target, and multilayer shielding

Monte Carlo program

This study's design of multilayer shielding was carried out by simulating the Monte Carlo method using the PHITS code. The simulation was conducted in two steps, the first was to get the layer composition of the shielding material with a fixed dimension, and the second was to get the optimum thickness with the previous simulation result. The source projectile parameters, energy, position, and beam direction are set in the source card input file. At the same time, the material composition and density are placed on the material and cell card. The geometry set was input on the cell and surface card. The simulation data for assessing shielding effectiveness are the effective dose and ambient dose equivalent of protons, neutrons, and photons obtained from the T-Track tally. The multiplier section will produce the effective dose and ambient dose rate by setting -202 and -200, respectively. The multiplier ID -200 is for H*(10), and -202 is for effective dose using conversion coefficient based on International Commission on Radiological Protection (ICRP) publications 103 and 116 [17].

Meanwhile, the fluence and energy spectrum of proton and neutron across the shielding material can be attained from the T-Cross tally. In addition, besides looking at neutrons and gamma dose equivalents, this study also estimates the induced radiation along shielding material with prediction of neutron capture and spallation reaction process. The number of particles in this simulation is 10^6, with maxcas 10^5 and maxbch 10^1. The simulation error is below 2%.

Definition and theory for the calculation of shielding measurement

According to the International Commission on Radiation Units and Measurements (ICRU) for area monitoring and shielding effectiveness measurement, the operational quantity for assessing effective dose is the ambient dose equivalent. A depth of 10 mm is recommended for strongly penetrating radiation, H*(10). Ambient dose equivalent, H*(10), is the dose equivalent produced by the corresponding expanded and aligned field in the ICRU sphere as a theoretical construct of material for tissue-equivalent at a depth of 10 mm on the radius opposing the direction of the aligned field. The ambient dose equivalent (Sv), H*(10), was measured on a monitor detector or survey meter. In addition, measurements can be made using a personal dosimeter to measure personal dose equivalent (Sv).

The calculation of these parameters follows the ICRP standard using the following equation [17,18]:

$$\phi = \frac{dN}{da} \quad (2.1)$$

where ϕ is a fluence (m^{-2}), the number of incident particles (dN) in a sphere of cross-sectional area (da). The rate of fluence or derivative fluence over time is called flux. Then an absorbed dose, D, is the average energy exposed by ionizing radiation to a mass of matter with the unit of J/kg, or gray (Gy):

$$D = \frac{d\bar{\varepsilon}}{dm} \quad (2.2)$$

$$H = DQ \quad (2.3)$$

$$H_T = \sum_R w_R D_{T,R} \quad (2.4)$$

$$E = \sum_T w_T \sum_R w_R D_{T,R} = \sum_T w_T H_T \quad (2.5)$$

where H is the equivalent dose at a point, D is the absorbed dose, and Q is the quality factor at that point. For the equivalent dose in an organ or tissue, H_T, is the mean absorbed dose to a tissue T by radiation R with a given weight factor w_R. Where the value of w_R for each type of radiation and energy range has been determined in ICRP publication 103 [18]. While the effective dose, E, is the equivalent dose in tissue or organ T times the tissue weighting factor, w_T. The unit of equivalent and effective dose is Sievert (Sv).

The ambient dose equivalent value is obtained by multiplying the dose conversion coefficient with the fluence[19]:

$$H*(10) = F\phi \quad (2.6)$$

where F is the conversion factor of fluence to ambient dose equivalent, H*(10), calculated using Monte Carlo simulation of the PHITS code system based on the ICRP standard.

RESULTS AND DISCUSSION

Effective dose and ambient dose equivalent

The simulation starts by bombarding protons on the target water, producing secondary radiation of neutrons and gamma rays. The shielding performance can be seen from the effective dose profile (Figure 3), the ambient dose equivalent profile along the depth of the shielding material (Figure 4), and the value of the ambient dose equivalent rate behind the shielding (Figure 5).

Figure 3 indicates that neutron radiation dominates, and the dose is much higher than gamma-ray radiation. From this profile, the combined structure of Fe-concrete-BPE and Fe-BPE-concrete has the highest effective dose at the beginning of the depth and then drops to almost zero after reaching 50 cm thickness. Because Fe material has a high inelastic cross-section value for fast neutrons, it can effectively attenuate fast neutrons, reduce their energy to intermediate neutrons, and produce a lot of gamma radiation. Therefore, the first layer has a high build-up factor. As a comparison, the combination of concrete-Fe-BPE and BPE-Fe-concrete has a total effective dose value close to zero at depths above 80 cm. And the rest, the variety of concrete-BPE-Fe and BPE-concrete-Fe, reached the lowest effective dose after 100 cm.

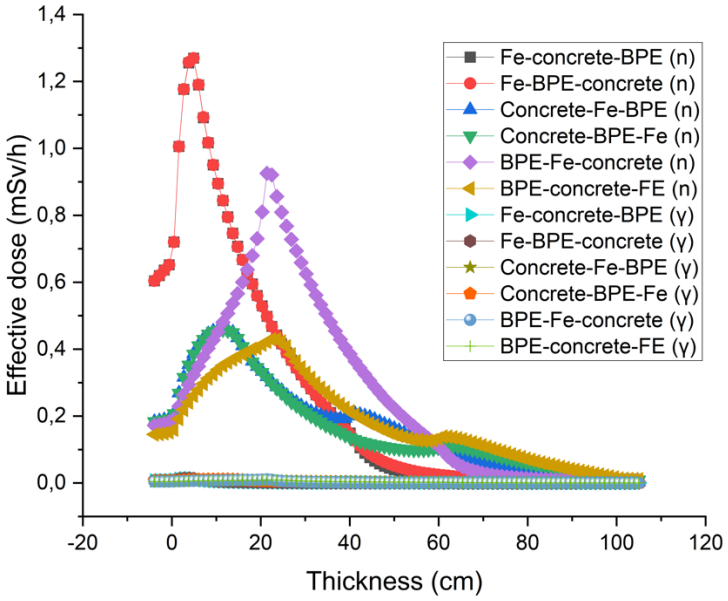

Figure 3. Effective dose profile in shielding depth for neutron and photon from high energy proton source of 230 MeV

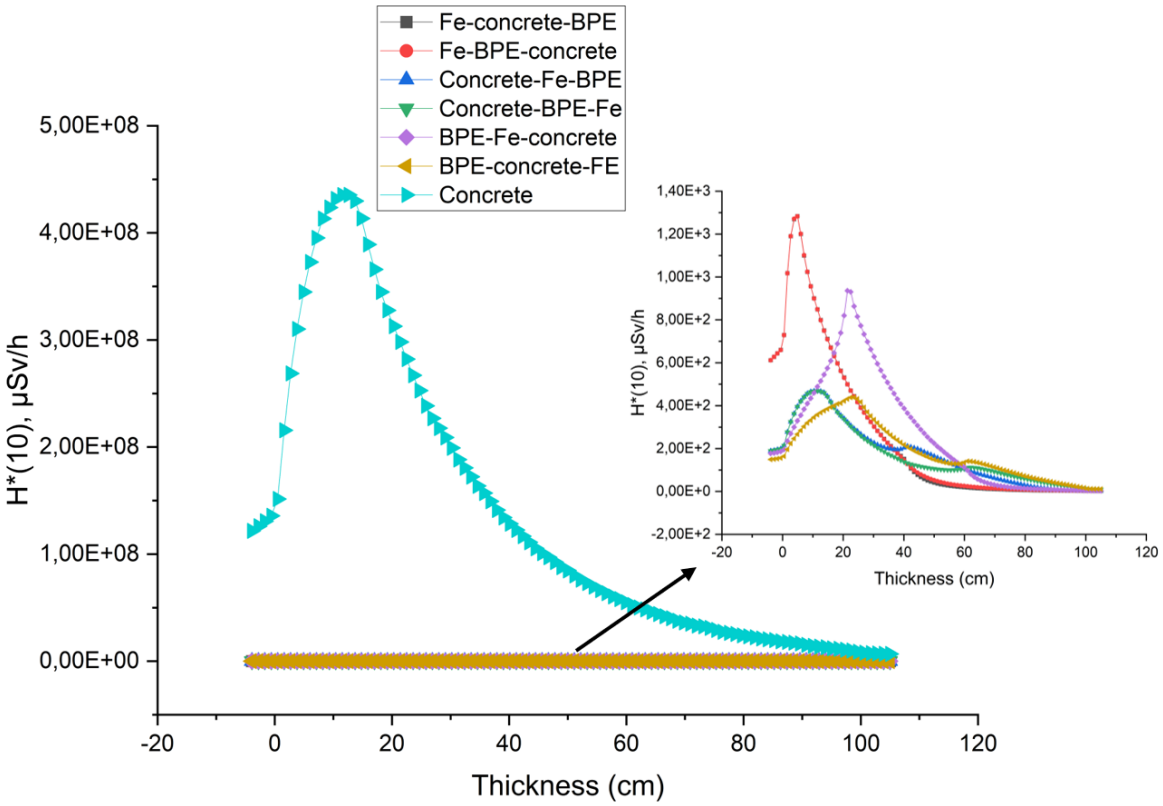

Figure 4. Ambient dose rate (H*(10) profile for different shielding scenarios

The simulation of the ambient dose equivalent rate along the shielding depth is shown in Figure 4. Multilayer shielding structure offers better performance than single layer from concrete materials with significantly lower ambient dose equivalent. While the

value of H*(10) behind the shielding for various multilayer scenarios is depicted in Figure 5. The configuration of Fe-concrete-BPE has the lowest ambient dose equivalent rate with a value of 2.436 mSv/h, slightly different from Fe-BPE-concrete which is 2.536 mSv/h. The second level is the configuration of BPE-Fe-concrete or Concrete-Fe-BPE, with a value range of 3.451 mSv/h and 3.753 mSv/h, respectively. Then the highest ambient dose H*(10) rate value is 10.929 mSv/h for the BPE-concrete-Fe layer.

The comparison results show that even though the combination of Fe-concrete-BPE has the lowest H*(10) rate, the scenario has a drawback on high emission of neutron and gamma-ray from the first layer. Therefore, the second configuration option can be chosen for a conservative design (BPE-Fe-concrete and Concrete-Fe-BPE).

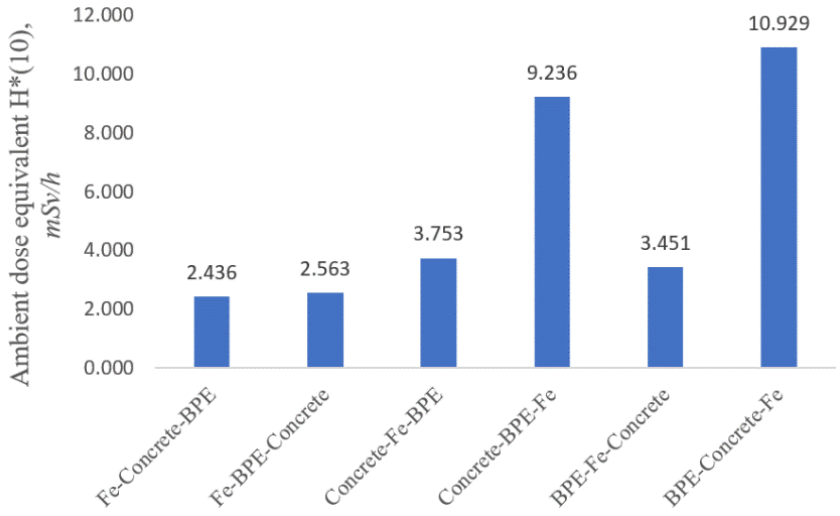

Figure 5. Ambient dose equivalent H*(10) rate of multilayer shielding design

Fluence distribution and spectrum energy across the surface

The radiation fluence distribution in the shielding depth generated by the MCNP PHITS code is shown in Figures 6, 7, and 8 while Figure 9 depicts the energy spectrum of protons and neutrons in each layer of the shielding material. The simulation findings confirm that the Fe material in the first layer is the most effective at lowering the energy of protons and neutrons. This is because Fe has a larger macroscopic cross-section for fast neutrons than concrete and BPE materials. The collision between the fast neutrons and the Fe nucleus produces an inelastic scattering reaction that causes a decrease of the neutron energy to the intermediate and thermal levels. On the other hand, the inelastic scattering reaction results in high neutron and gamma-ray emission in the Fe layer (see Fig. 3). Therefore, it will cause consideration of the additional neutron and gamma-ray exposure to the patient from the Fe scattering effect. For comparison, the configuration of concrete or BPE in the first layer gives lower neutron and gamma-ray radiation, though some structures have higher doses behind the shielding. Hydrogenous material (concrete) and composite (BPE) can attenuate intermediate neutrons and absorb thermal neutrons & gamma rays readily. Based on the visualization above, using Fe in the second layer after concrete or BPE and avoiding putting the Fe at the end of the layer can reduce radiation exposure to people

inside the gantry room while maintaining a relatively low ambient dose equivalent value.

Induced radiation analysis

Long-term activation of the shielding materials becomes a burden when the facility is decommissioned after many years of operation [20]. The induced radiation analysis strongly depends on the shielding materials composition, as listed in Table 1. Analysis of radioactivity activation was predicted using nuclear cross-section data from a TALYS-based evaluated nuclear data library (TENDL 2019)[21]. Several activated elements are indicated during the operation of proton radiation therapy by the secondary fast neutron radiation bombardment to concrete, iron, and BPE. The prediction of activated radioisotope data, half-life, and decay mode are shown in Table 3, including additional data from previous work.

Secondary neutron radiation from high-energy proton exposure can activate many elements in shielding materials. The activation reaction can result from neutron capture (n,γ), which produces heavier elements and gamma emission, or from neutron spallation [(n,α), (n,p), (n,d), and (n,nα)] which generates lighter atomic products. Radioactive isotopes with short and long lives are derived from the prediction of induced radiation. A short-lived radioisotope is one whose half-life is measured in seconds, minutes, or hours. The short-lived radioisotope predicted are ^{56}Mn, ^{57}Mn, ^{28}Al, ^{29}Al, ^{30}Al, ^{31}Si, ^{27}Mg, ^{41}Ar, ^{43}K, ^{44}K, ^{16}N, ^{12}B, ^{8}Be, ^{11}Be, ^{24}Na, and ^{8}Li. While the long-lived radioisotopes predicted consist of ^{55}Fe, ^{51}Cr, ^{53}Mn, ^{54}Mn, ^{41}Ca, ^{37}Ar, ^{40}K, ^{45}Ca, and ^{10}Be. Several heavy elements in concrete, such as Eu, Co, and Cs, have the potential to be activated despite their small proportion in the composition. Carrol predicted the activation of these heavy elements in a prior study that generated long-lived radioactive of ^{152}Eu, ^{154}Eu, ^{60}Co, and ^{134}Cs.

Table 3. Prediction of neutron activation in shielding materials

Elements in shielding material	Possible nuclear reaction	Isotope	Half life	Decay mode	Principal γ's, β's, X-ray's keV (%)
Fe (^{56}Fe (91.75%), ^{54}Fe (5.85%), ^{57}Fe (2.12%)	^{56}Fe(n,γ)^{57}Fe	^{57}Fe	-	stable	-
	^{56}Fe(n,α)^{53}Cr	^{53}Cr	-	stable	-
	^{56}Fe(n,p)^{56}Mn	^{56}Mn	2.6 h	β^-	β- 1216.85 (56.6%), 381.96 (27.5%), 255.23 (14.5%), 99.15 (1.2%) γ 846.764 (98.9%), 1810.726 (26.9%), 2113.092

Elements in shielding material	Possible nuclear reaction	Isotope	Half life	Decay mode	Principal γ's, β's, X-ray's keV (%)
					(14.2%), 2523.06 (1.0%)
	$^{56}Fe(n,d)^{55}Mn$	^{55}Mn	-	stable	
	$^{56}Fe(n,n\alpha)^{52}Cr$	^{52}Cr	-	Stable	
	$^{54}Fe(n,\gamma)^{55}Fe$	^{55}Fe	2.744 y	ec decay	γ: 126.0 ($1.28x10^{-7}$%) X-ray: 5.899 (16.6%), 5.888 (8.5%), 6.489 (3.4%), 0.556 (0.7%)
	$^{54}Fe(n,\alpha)^{51}Cr$	^{51}Cr	27.7 d	ec decay	γ: 320.083 (9.91%) X-ray: 4.952 (19.8%), 5.426 (4.4%), 0.446 (0.6%)
	$^{54}Fe(n,p)^{54}Mn$	^{54}Mn	312.2 d (~ 0.85 y)	ec β+	γ: 834.848 (99.98%) X-ray: 5.415 (15%), 5.406 (7.7%), 5.946 (6%), 0.50 (0.65%) β+ (<5.7E-7 %), β- 239.7 (0.000093 %)
	$^{54}Fe(n,d)^{53}Mn$	^{53}Mn	$3.7 x10^{6}$ y	ec decay	X-ray: 5.415 (15%), 5.406 (7.7%), 5.946 (6%), 0.50 (0.65%)
	$^{54}Fe(n,n\alpha)^{50}Cr$	^{50}Cr		Stable	
	$^{57}Fe(n,\gamma)^{58}Fe$	^{58}Fe		Stable	
	$^{57}Fe(n,\alpha)^{54}Cr$	^{54}Cr		Stable	
	$^{57}Fe(n,p)^{57}Mn$	^{57}Mn	85.4 s	β^-	β- 1135 (75%), 1077 (15%), 809 (6.3%), 968 (2.2%), 393 (1.1%) γ

Elements in shielding material	Possible nuclear reaction	Isotope	Half life	Decay mode	Principal γ's, β's, X-ray's keV (%)
					122.063 (14%), 14.413 (11%), 692.0 (5.5%), 352.32 (2.1%) X-ray: 6.404 (16.3%), 6.391 (8.3%), 7.056 (6.7%), 0.615 (0.73%)
	$^{57}Fe(n,d)^{56}Mn$	^{56}Mn	2.6 h	β^-	β- 1216.85 (56.6%), 381.96 (27.5%), 255.23 (14.5%), 99.15 (1.2%) γ 846.764 (98.9%), 1810.726 (26.9%), 2113.092 (14.2%), 2523.06 (1.0%)
	$^{57}Fe(n,n\alpha)^{53}Cr$	^{53}Cr		stable	
Concrete					
^{28}Si (92.2%), ^{29}Si (4.7%), ^{30}Si (3.1%)	$^{28}Si(n,\gamma)^{29}Si$	^{29}Si		Stable	
	$^{28}Si(n,\alpha)^{25}Mg$	^{25}Mg		Stable	
	$^{28}Si(n,p)^{28}Al$	^{28}Al	2.3 min	β^-	β- 1241.8 (99.99%), γ 1778.99 (100%)
	$^{28}Si(n,d)^{27}Al$	^{27}Al		Stable	
	$^{28}Si(n,n\alpha)^{24}Mg$	^{24}Mg		Stable	
	$^{29}Si(n,\gamma)^{30}Si$	^{30}Si		stable	
	$^{29}Si(n,\alpha)^{26}Mg$	^{26}Mg		stable	

Elements in shielding material	Possible nuclear reaction	Isotope	Half life	Decay mode	Principal γ's, β's, X-ray's keV (%)
	$^{29}Si(n,p)^{29}Al$	^{29}Al	6.56 min	β^-	β- 1023.7 (89.9%), 490.1 (6.3%), 670.4 (3.8%) γ 1273.36 (91.3%), 2425.73 (5.2%), 2028.09 (3.5%), 1152.57 (1.03%)
	$^{29}Si(n,d)^{28}Al$	^{28}Al	2.3 min	β^-	β- 1241.8 (99.99%), γ 1778.99 (100%)
	$^{29}Si(n,n\alpha)^{25}Mg$	^{25}Mg		Stable	
	$^{30}Si(n,\gamma)^{31}Si$	^{31}Si	157.24 min = 2.6 h		β- 595.93 (99.95%), γ 1266.1 (0.0554%)
	$^{30}Si\ (n,\alpha)^{27}Mg$	^{27}Mg	9.5 min	β^-	β- 724.8 (70.9%), 646.3 (29%) γ 843.76 (71.8%), 1014.52 (28.2%)
	$^{30}Si(n,p)^{30}Al$	^{30}Al	3.62 s	β^-	β- 2311 (67.3%), 2932 (17.1%), 1661 (6.6%),1671 (5.7%), 1467 (2.6%)
	$^{30}Si(n,d)^{29}Al$	^{29}Al	6.56 min	β^-	β- 1023.7 (89.9%), 490.1 (6.3%), 670.4 (3.8%) γ

Elements in shielding material	Possible nuclear reaction	Isotope	Half life	Decay mode	Principal γ's, β's, X-ray's keV (%)
					1273.36 (91.3%), 2425.73 (5.2%), 2028.09 (3.5%), 1152.57 (1.02%)
	$^{30}Si(n,n\alpha)^{26}Mg$	^{26}Mg		Stable	
^{40}Ca (96.94%), ^{44}Ca (2.086%)	$^{40}Ca(n,\gamma)^{41}Ca$	^{41}Ca	9.94×10^4 y	ec decay	X-ray 3.314 (7.6%), 3.311 (3.8%), 3.591 (2.7%), 0.259-0.362 (0.3%)
	$^{40}Ca(n,\alpha)^{37}Ar$	^{37}Ar	35.011 d	ec decay	X-ray 2.623 (5.5%), 2.621 (2.8%), 2.816 (1.4%), 0.181-0.264 (0.2%)
	$^{40}Ca(n,p)^{40}K$	^{40}K	1.248×10^9 y	β^-	β- 560,18 (89.27%), γ 1460.82 (10.66%),
	$^{40}Ca(n,d)^{39}K$	^{39}K		stable	
	$^{40}Ca(n,n\alpha)^{36}Ar$	^{36}Ar		Stable	
	$^{44}Ca(n,\gamma)^{45}Ca$	^{45}Ca	162.61 d (~0.44 y)	β^-	β- 76.9 (100%), γ 12.40 (0.0000045 %),
	$^{44}Ca(n,\alpha)^{41}Ar$	^{41}Ar	109.61 min (1.8 h)	β^-	β- 459.36 (99.16%), γ 1293.64 (99.16%),
	$^{44}Ca(n,p)^{44}K$	^{44}K	22.13 min	β^-	β- 2601 (34%), 990 (28.5%), 816 (11%), 481 (7.2%) γ

Elements in shielding material	Possible nuclear reaction	Isotope	Half life	Decay mode	Principal γ's, β's, X-ray's keV (%)
					1157 (58%), 2150.79 (23%), 2518.99 (9.7%), 1499.45 (7.8%), 1126.1 (7.6%), 1024.74 (6.7%), 3661.37 (6.1%), 1752.63 (4.1%)
	$^{44}Ca(n,d)^{43}K$	^{43}K	22.3 h	β^-	β- 304.85 (90.9%), 476.65 (4.0%), 143.1 (2.6%), 769.2 (1.5%) γ 372.76 (86.8%), 617.49 (79.2%), 396.86 (11.9%), 593.39 (11.3%), 220.63 (4.8%), 1021.7 (2%)
	$^{44}Ca(n,n\alpha)^{40}Ar$	^{40}Ar		Stable	
^{16}O	$^{16}O(n,\gamma)^{17}O$	^{17}O		Stable	
	$^{16}O(n,\alpha)^{13}C$	^{13}C		Stable	
	$^{16}O(n,p)^{16}N$	^{16}N	7.13 s	β^-	β- 1941,7 (66.2%), 4979.8 (28%), 1461.6 (4.8%), 630.6 (1%) γ 6128.6 (67%), 7115.2 (5%),
	$^{16}O(n,d)^{15}N$	^{15}N		Stable	

Elements in shielding material	Possible nuclear reaction	Isotope	Half life	Decay mode	Principal γ's, β's, X-ray's keV (%)
	$^{16}O(n,n\alpha)^{12}C$	^{12}C		Stable	
^{12}C	$^{12}C(n,\gamma)^{13}C$	^{13}C		Stable	
	$^{12}C(n,\alpha)^{9}Be$	^{9}Be		Stable	
	$^{12}C(n,p)^{12}B$	^{12}B	20.2 ms	β^-	β- : 6438.7 (98.2%), γ : 4438.9 (1.2%)
	$^{12}C(n,d)^{11}B$	^{11}B		Stable	
	$^{12}C(n,n\alpha)^{8}Be$	^{8}Be	770 ms	ec β+	β+ : 6732 (>88%)
^{27}Al	$^{27}Al(n,\gamma)^{28}Al$	^{28}Al	2.3 min	β^-	β- 1241.8 (99.99%), γ 1778.99 (100%)
	$^{27}Al(n,\alpha)^{24}Na$	^{24}Na	15 h	β^-	β- 554.1 (99.86%), γ 1368.6 (99.99%), 2754.0 (99.86%)
	$^{27}Al(n,p)^{27}Mg$	^{27}Mg	9.5 min	β^-	β- 724.8 (70.9%), 646.3 (29%) γ 843.76 (71.8%), 1014.52 (28.2%)
	$^{27}Al(n,d)^{26}Mg$	^{26}Mg		Stable	
	$^{27}Al(n,n\alpha)^{23}Na$	^{23}Na		Stable	
BPE (H,O,and C isotppe reaction prediction is same as in concrete) ^{10}B	$^{10}B(n,\gamma)^{11}B$	^{11}B		Stable	
	$^{10}B(n,\alpha)^{7}Li$	^{7}Li		Stable	
	$^{10}B(n,p)^{10}Be$	^{10}Be	$1.51x10^{6}$ y	β^-	β- : 202.6 (100%)

Elements in shielding material	Possible nuclear reaction	Isotope	Half life	Decay mode	Principal γ's, β's, X-ray's keV (%)
	$^{10}B(n,d)^{9}Be$	^{9}Be		Stbale	
	$^{10}B(n,n\alpha)^{6}Li$	^{6}Li		Stable	
^{11}B	$^{11}B(n,\gamma)^{12}B$	^{12}B	20.2 ms	β^-	β- 6438.7 (98.2%) γ 4438.9 (1.2%)
	$^{11}B(n,\alpha)^{8}Li$	^{8}Li	839.9 ms	β^-	β- : 6248 (100%)
	$^{11}B(n,p)^{11}Be$	^{11}Be	13.76 s	β^-	β- 5516.5 (54.7%), 4461.5 (31.4%, 2155.2 (6.5%) γ 477.6 (0.39%)
	$^{11}B(n,d)^{10}Be$	^{10}Be	$1.51x10^{6}$ y	β^-	β- : 202.6 (100%)
	$^{11}B(n,n\alpha)^{7}Li$	^{7}Li		Stable	
Long-lived radioactive predicted in previous work from concrete in a cyclotron vault [20]					
^{151}Eu	$^{151}Eu(n,\gamma)^{152}Eu$	^{152}Eu	13.4 y	ec β+	γ 122 (37%), 344 (27%) 779 (14%), 960 (15%) 1087 (12%), 1110 (14%) 1408 (22%)
^{153}Eu	$^{153}Eu(n,\gamma)^{154}Eu$	^{154}Eu	8.5 y	β^-	γ 120 (38%), 720 (21%) 1000 (31%), 1278 (37%)
^{59}Co	$^{59}Co(n,\gamma)^{60}Co$	^{60}Co	5.27 y	β^-	γ 1173 (100%), 1332 (100%) β- : 95.77 (100%)

Elements in shielding material	Possible nuclear reaction	Isotope	Half life	Decay mode	Principal γ's, β's, X-ray's keV (%)
^{133}Cs	$^{133}Cs(n,\gamma)^{134}Cs$	^{134}Cs	2.065 y	β^-	γ 605 (98%), 796 (99%), 570 (23%)

The optimum thickness of multilayer shielding design for protection radiation purposes

The first simulation found that the BPE-Fe-concrete or Concrete-Fe-BPE layer arrangement was an excellent combination compared to other multilayer shielding arrangements. Further simulations were carried out to obtain the optimum thickness of each layer by referring to the radiation safety standard, namely 1 mSv/year [22]. Simulation is done by varying the Fe, concrete, and BPE thickness. The maximum thickness of Fe is 100 cm, and the BPE is maintained at 20-30 cm. The shielding distance was changed from 10 cm to 100 cm following the shielding wall and the source distance in the gantry room. Ambient dose H*(10) rate values for various thicknesses of shielding materials are shown in Table 4. The data was derived from an irradiation time of around 1 h. From these data, the optimum thickness of Fe-concrete-BPE multilayer shielding is 90-90-20 cm, with an H*(10) value of approximately 8.384 μSv/h. However, the Fe-concrete-BPE thickness of 100-80-20 cm has a lower dose rate of 6.418 μSv/h. The ambient dose value for the variation of 90-90-20 cm is comparable to shielding 1-layer concrete with a thickness of 330 cm. So, the Fe-concrete-BPE multilayer shielding can reduce the shielding thickness by up to 40%.

For the BPE-Fe-concrete combination, the thickness of 20-90-110 cm has the same H*(10) value as 300 cm concrete. This multilayer scenario can decrease the thickness by around 27%. While 30-90-100 cm of this combination can reach the shielding target. The combination of Concrete-Fe-BPE demonstrates a comparable design. Thus, the thickness of the concrete (110 cm), Fe (90 cm), and BPE (30 cm) can generate a safe shielding design following regulations by placing Fe in the middle layer between the concrete material and BPE.

Table 4. Ambient dose rate H*(10) for variation of shielding material thickness

Material	Thickness (cm)	H*(10), μSv/h	Standard [22]
Fe-concrete-BPE	100-80-20 à 200	6.418	10 μSv/h
Fe-concrete-BPE	90-90-20 à 200	8.384	
Fe-concrete-BPE	80-100-20 à 200	20.313	
BPE-Fe-concrete	20-80-100 à 200	20.468	
BPE-Fe-concrete	20-90-110 à 220	13.895	
BPE-Fe-concrete	30-90-110 à 230	7.071	
Concrete-Fe-BPE	100-80-20 à 200	41.554	
Concrete-Fe-BPE	100-90-30 à 220	14.740	
Concrete-Fe-BPE	110-90-30 à 230	6.261	
comparison with 1 layer shielding:			
concrete	300	13.926	
concrete	330	10.159	

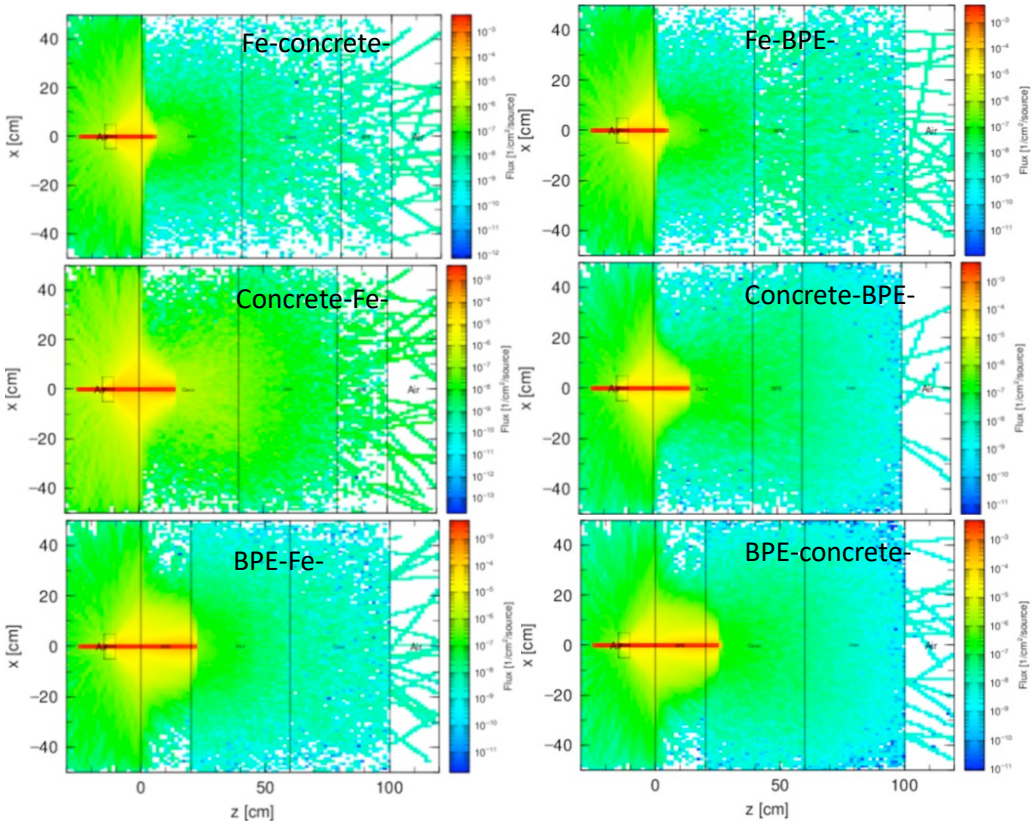

Figure 6. Fluence distribution map of proton in shielding depth

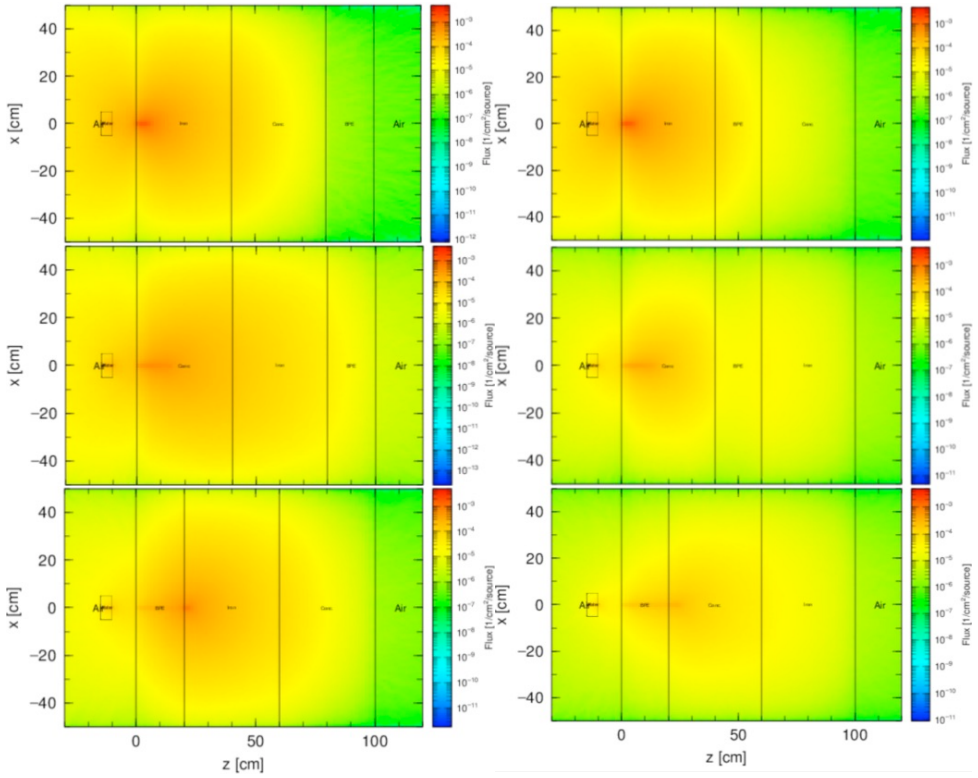

Figure 7. Fluence distribution map of neutron in shielding depth

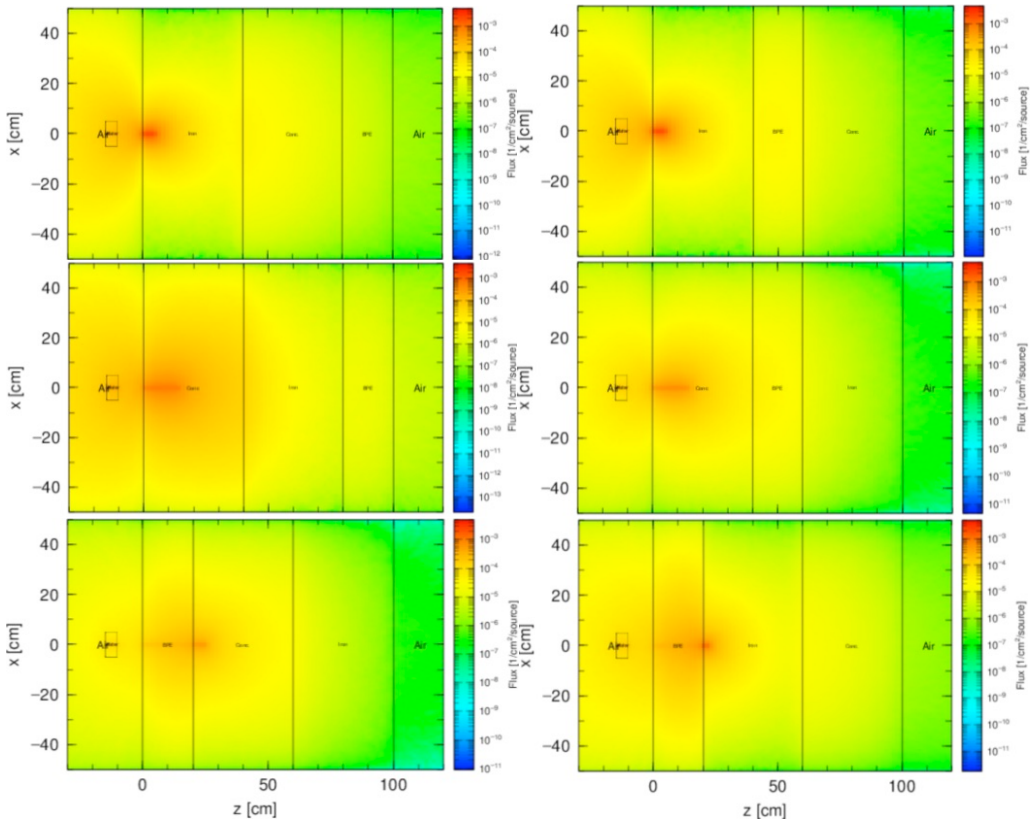

Figure 8. Fluence distribution map of photon in shielding depth

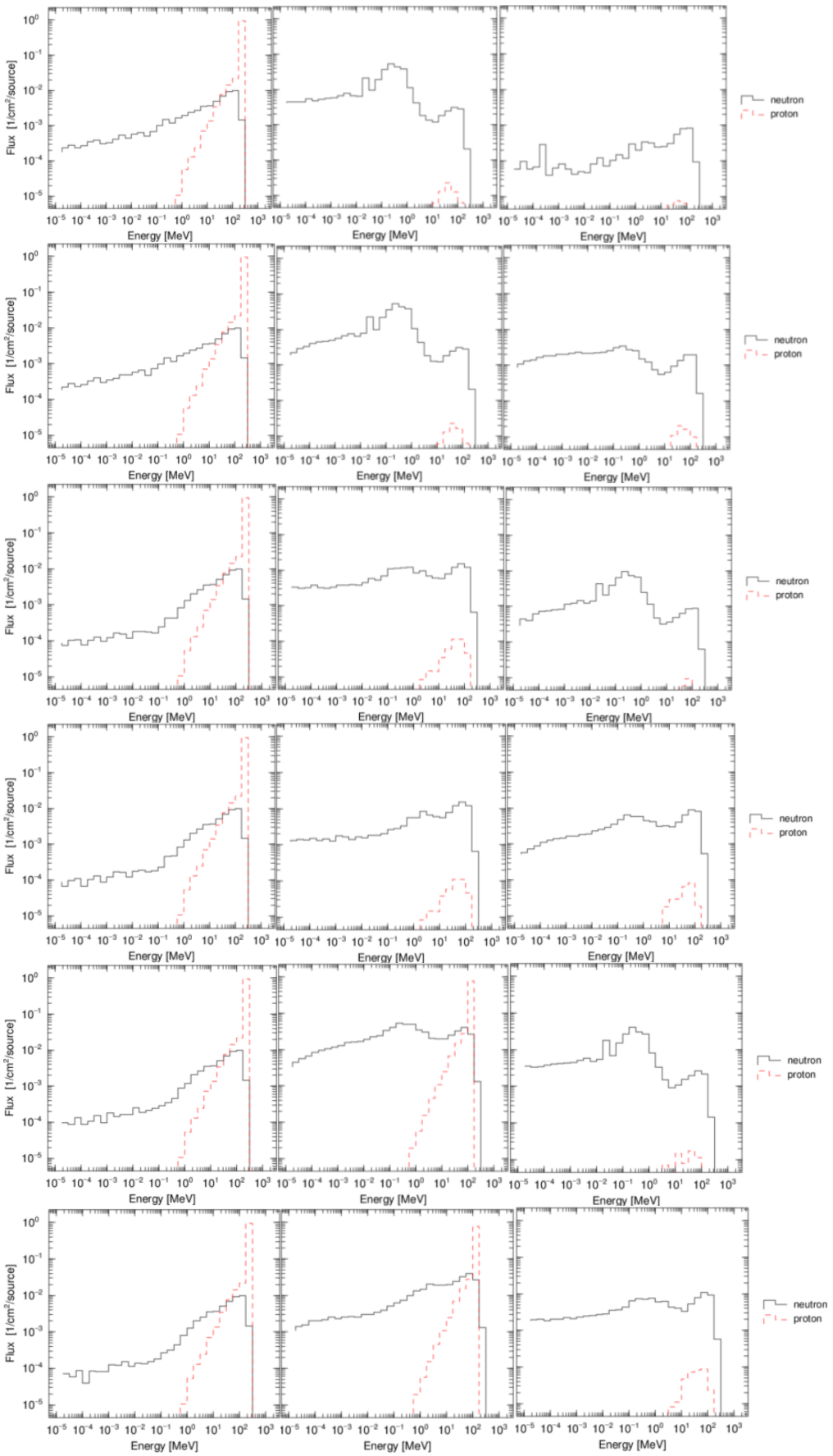

Figure 9. Energy spectrum of proton and neutron across the material of shielding region (total thickness=100 cm, Fe=40 cm, concrete=40 cm, BPE=20 cm)

CONCLUSIONS

A new combination of structure and composition of multilayer shielding from the metal-hydrogenous-composite material is suitable against proton, neutron, and gamma-ray radiation. The fluence distribution map illustrates that the proton penetrating power is lowest in the Fe material in the first layer and the most penetrating power in the BPE material. The Fe material is superior in reducing the high energy of proton and neutron but has a high build-up factor with higher photon emission. Therefore, placing Fe in the first layer will cause additional gamma exposure to the people inside the gantry room even though the ambient dose equivalent, H*(10), is the lowest. The combination of BPE-Fe-concrete or Concrete-Fe-BPE performs better than another scenario with relatively minimum H*(10) and less build-up effect. By referring to the ICRP recommendation standard of ambient dose equivalent rate, the multilayer shielding scenario can reduce the thickness by up to 40% from the Fe-concrete-BPE combination and 27% from BPE-Fe-concrete/Concrete-Fe-BPE. Then the optimum thickness of each layer is BPE (30 cm), Fe (90 cm), and concrete (110 cm) by placing Fe between concrete and BPE. While the activation analysis on the shielding material showed that there were short-lived and long-lived isotopes predicted from secondary neutron bombardment. The short-lived radioisotope predicted are ^{56}Mn, ^{57}Mn, ^{28}Al, ^{29}Al, ^{30}Al, ^{31}Si, ^{27}Mg, ^{41}Ar, ^{43}K, ^{44}K, ^{16}N, ^{12}B, ^{8}Be, ^{11}Be, ^{24}Na, and ^{8}Li. While the long-lived radioisotopes predicted consist of ^{55}Fe, ^{51}Cr, ^{53}Mn, ^{54}Mn, ^{41}Ca, ^{37}Ar, ^{40}K, ^{45}Ca, and ^{10}Be. From the previous study, certain long-lived radioactive elements such as ^{152}Eu, ^{154}Eu, ^{60}Co, and ^{134}Cs were also predicted to be present in concrete shielding.

ACKNOWLEDGMENTS

The authors would like to thank Universiti Sains Malaysia (USM) and Universitas Gadjah Mada (UGM) for providing research facilities, and the Malaysian government for financial support through the Malaysia International Scholarship (MIS) program and the National Research and Innovation Agency of Indonesia (BRIN).

REFERENCES

[1] M.T. Prusator, S. Ahmad, Y. Chen (2018). Shielding verification and neutron dose evaluation of the Mevion S250 proton therapy unit, *J. Appl. Clin. Med. Phys*. **19**, 305.

[2] R.A. Hälg, U. Schneider (2020). Neutron Dose and its Measurement in Proton Therapy-Current State of Knowledge, *Br. J. Radiol.* **9393**(1107), 20190412.

[3] F. Aliyah, S.G. Pinasti, A.A. Rahman (2021). Proton therapy facilities: An overview of the development in recent years, *IOP Conf. Ser. Earth Environ. Sci.* **927**, 012042.

[4] W.D. Newhauser, R. Zhang (2015). The physics of proton therapy, *Phys. Med. Biol.* **60**, R155–R209.

[5] H. Paganetti (2019). *Proton Therapy Physics*, 2nd ed. Series in Medical Physics and Biomedical Engineering, 2nd ed. CRC Press, Taylor & Francis Group, Boca Raton, New York.

[6] G. Hu, H. Hu, S. Wang, H. Han, Y. Otake, Z. Pan, A. Taketani, H. Ota, T. Hashiguchi, M. Yan (2017). New shielding material development for compact accelerator-driven neutron source, *AIP Adv*. **7**, 045213.

[7] B.L. Lai, Y.S. Huang, P.C. Lai, W.H. Chu, R.J. Sheu (2020). Comparison of different methods for the shielding analysis of an AB-BNCT facility based on the Be(p,xn) reaction with 30-MeV protons, *Appl. Radiat. Isot.* **166**, 109351.
[8] J.L. Wang, L.A. Cruz, Q.B. Wu, Q. Wang, Y. Wei, H.K. Wang (2020). Radiation shielding design of a compact single-room proton therapy based on synchrotron, *Nucl. Sci. Tech.* **31**, 1.
[9] G. Hu, G. Shi, H. Hu, Q. Yang, B. Yu, W. Sun (2020). Development of gradient composite shielding material for shielding neutrons and gamma rays, *Nucl. Eng. Technol.* **52**, 2387.
[10] G. Hu, H. Hu, Q. Yang, B. Yu, W. Sun, (2020). Study on the design and experimental verification of multilayer radiation shield against mixed neutrons and γ-rays, *Nucl. Eng. Technol.* **52**, 178.
[11] R.S. Augusto, A. Trudel, Z. Liu, M. Kinakin, W. Paley, Z. Bjelić, A. Messenberg, (2021). An overview of the shielding optimization studies for the TRIUMF-ARIEL facility, *Nucl. Inst. Methods Phys. Res. A*. **1005**, 165401.
[12] G.F. Garcia-Fernandez, E. Gallego, J.M. Gomez-Ros, H.R. Vega-Carrillo, R. Garcia-Baonza, L.E. Cevallos-Robalino, K.A. Guzman-Garcia (2021). Neutron dosimetry and shielding verification in commissioning of Compact Proton Therapy Centers (CPTC) using MCNP6.2 Monte Carlo code, *Appl. Radiat. Isot.* **169**, 116.
[13] B. Ma, L. Song, M. Yan, Y. Ikeda, Y. Otake, S. Wang (2021). Multiobjective Optimization Shielding Design for Compact Accelerator-Driven Neutron Sources by Application of NSGA-II and MCNP, *IEEE Trans. Nucl. Sci.* **68**, 110.
[14] S.J. Frank and X.R. Zhu (2021). *Proton Therapy: Indications, Techniques and Outcomes*, 1st ed. Elsevier, Philadelphia.
[15] O. Ardenfors (2018). Out-of-field doses from proton therapy and doses from CBCT imaging: Risk of radiation-induced second cancer from modern radiotherapy, Stockholm University, 2018. https://www.diva-portal.org/smash/get/diva2:1256301/FULLTEXT01.pdf.
[16] B. Ma, Y. Otake, S. Wang, H. Sunaga, Y. Yamagata, A. Taketani, H. Hu, Q. Jia, G. Hu, U. Bautista (2018). Shielding design of a target station and radiation dose level investigation of proton linac for a compact accelerator-driven neutron source applied at industrial sites, *Appl. Radiat. Isot.* **137**, 129.
[17] ICRP (2010). *Conversion Coefficients for Radiological Protection Quantities for External Radiation Exposures.* ICRP Publication 116, Ann. ICRP. **40**, 2.
[18] ICRP (2007). International Commission on Radiological Protection, ICRP Publication 103- The 2007 Recommendations of the International Commission on Radiological Protection, UK.
[19] R. Casanovas, E. Prieto, M. Salvadó (2016). Calculation of the ambient dose equivalent H*(10) from gamma-ray spectra obtained with scintillation detectors, *Appl. Radiat. Isot.* **118**, 154.
[20] L.R. Carroll (2001). Predicting long-lived, neutron-induced activation of concrete in a cyclotron vault, Am. Inst. Phys. **576**, 301-304.
[21] A.J. Koning, D. Rochman, J.C. Sublet, N. Dzysiuk, M. Fleming, S. van der Marck (2019). TENDL: Complete Nuclear Data Library for Innovative Nuclear Science and Technology, *Nucl. Data Sheets* **155**, 1.
[22] A.D. Wrixon (2008). New ICRP recommendations, *J. Radiol. Prot.* **28**, 161.